CFD Simulation of a Isothermal Water Flow in the EADF-target Geometry in Dynamical Similarity (COULI Experiment)

L. Maciocco, L. Sorrentino

17 July 2001

Abstract

The results of the numerical simulation of an isothermal water-flow in a geometry typical of the spallation target of the Energy Amplifier Demonstration Facility (EADF) are presented, and compared with the experimental results obtained at CEA-Cadarache (COULI experiment).

All the calculations were performed with the Star-CD finite-volume commercial code. Basically, a 2D axisymmetric model was adopted, although a full 3D simulation was carried out as well, as explained below. The Chen k-ε high-Reynolds model was used, joined with a Norris & Reynolds Two-Layer model for the simulation of the near-wall turbulence.

The grid-independence of the solution has been verified, and the results obtained with two different convection schemes (QUICK and MARS) has been compared, in order to minimise numerical uncertainties. No appreciable differences were found in the results.

Because of the fact that experimental measurements revealed a high non-axisymmetric and non-stationary flow behaviour, the possible presence of instabilities intrinsic in the flow topology has been analysed through a full 3D simulation, obtained with the circumferential extrusion of the 2D model. The simulation yielded a steady solution, with results in perfect agreement with the 2D case. It is worth to notice that it was possible to obtain a converged solution in the 3D case only using the MARS scheme, while the QUICK scheme had numerical problems.

In spite of the above-mentioned lack of axial symmetry in the experimental set-up, the comparison with computational results showed the capability of Star-CD to correctly simulate the main flow characteristics.

Contents

1 Introduction

The task of the COULI benchmark is the analysis of the capability of turbulence models of simulating a flow configuration typical of the spallation region of the Energy Amplifier Demonstration Facility (EADF) window-type target [1]. This type of target is also considered as the reference one in the framework of the PDS-XADS European project.

The COULI experiment is being carried out at CEA Grenoble. The dimensions of the circuit are scaled by a factor 1/1.4, in geometrical similarity with the EADF target geometry. The experiment is performed with water in isothermal conditions, in fluid dynamic similarity with the Pb-Bi flow in the EADF target.

A proposal for the COULI benchmark has already been issued in November 1999 [2] and a set of preliminary calculations was carried out by CRS4 and FZK and a report issued in January 2000 [3]. Results revealed the presence of a boundary layer detachment in the diverging part of the duct, as it was confirmed later by experimental observation. However, the position and shape of the detachment was shown to be strongly dependent on the turbulence model used, confirming the strong need for a benchmarking activity on this kind of flow topology. An updated proposal has been issued in June 2002 [4], where a strategy for a co-ordinated activity of the participant to the COULI benchmark has been proposed on the basis of the latest experimental results obtained at CEA.

2 Test case set-up

2.1 Description

The geometry of the COULI test case is shown in Figure 1. Water flows along a circular pipe up to an hemispherical wall (window), where it is deviated along a converging-diverging duct, ending in an annular duct. The main flow characteristics are the stagnation point on the window and a flow detachment in the diverging duct.

Experiments have been carried out with water in isothermal conditions (T = 30 °C); the corresponding physical properties are reported in Table 1. Measurements are available for three flow-rate conditions with similar Reynolds number [4]. Only one regime was selected for the benchmark purpose, as reported in Table 2. Experimental LDV measurements of velocity and velocity fluctuation components were performed in sections A-1, B-2, M (originally this section was not considered) C-3, D8 and E9 (see Figure 2). Data in sections A-1 and B-2 are used to set and check the inlet boundary conditions. No experimental measurements were possible in the actual diverging duct, due to optical LDV problems related to the surface curvature.

Table 1 - Water physical properties at $T = 30$ °C.

Density ρ (Kg/m^3)	995.62
Viscosity μ (Kg/ms)	7.985×10^{-4}
Cinematic viscosity ν (m^2/s)	8.02×10^{-7}

Table 2 - Experimental conditions.

Flow rate, q (m^3/h)	Mean inlet velocity, U (m/s)	Re
105	3.714	4.63×10^5
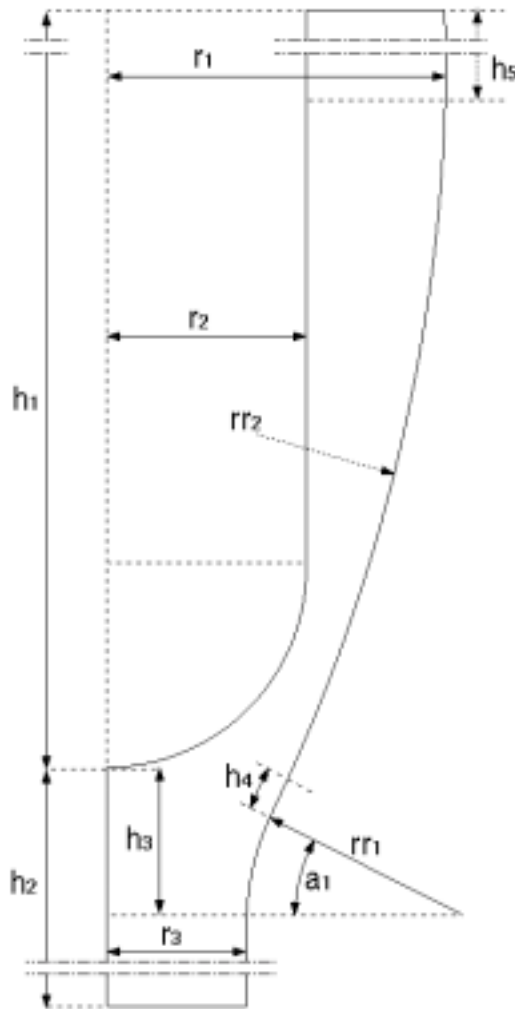
Parameter	Value
h_1 (mm)	1000
h_2 (mm)	1026.5
h_3 (mm)	57.14
h_4 (mm)	7.14
h_5 (mm)	(h_1-257.91)
r_1 (mm)	121.43
r_2 (mm)	71.43
r_3 (mm)	50
rr_1 (mm)	95.71
a_1 (deg)	25
rr_2 (mm)	(634.4)

Figure 1 - Geometry of the COULI benchmark (the number in brackets can be deduced from the other dimensions).
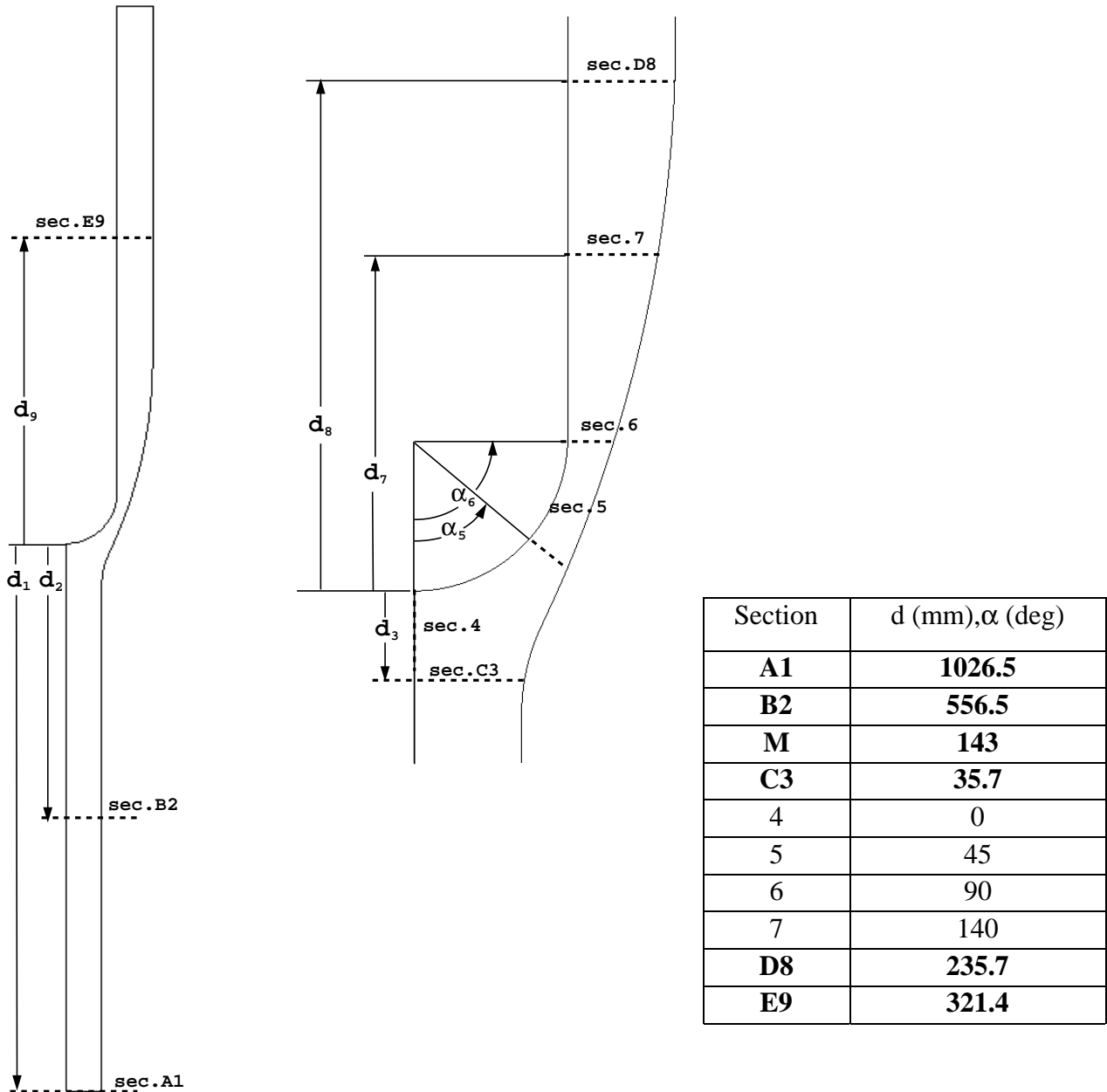
Section	d (mm),α (deg)
A1	**1026.5**
B2	**556.5**
M	**143**
C3	**35.7**
4	0
5	45
6	90
7	140
D8	**235.7**
E9	**321.4**

Figure 2 - Position of the probe sections for boundary conditions setting and results comparison. Sections are drawn on the actual computational domain. Experimental measurements are available in sections A-1, B-2, M (not drawn in the figure), C-3, D8 and E9.

2.2 Numerical set-up and boundary conditions

The computational domain is shown in Figure 2. The outlet duct is 1 m long, as prescribed in the benchmark proposal in order to avoid effects of the outlet condition on the region of interest. Both 2D axisymmetric and full 3D models were used (see Sec. 3.5).

A picture of the computational mesh in the window region is shown in Figure 3. Basically, hexahedral elements were used in the whole domain, although some prismatic elements are present on the axis and in the diverging duct, in order to allow a similar mesh density in the throat and in the riser. The total number of cells is 25,487 for cases 1 and 3, 101,948 for case 2 and 1,835,064 for case 4 (see Table 3).

Inlet boundary conditions were set according to velocity and velocity fluctuation measurements in section A-1. Radial and tangential velocity components were considered negligible. The inlet profile of turbulence dissipation ε was deduced from the relation

$$\varepsilon = C_\mu^{3/4} \frac{k^{3/2}}{L_t}$$

($C_\mu = 0.09$) with the assumption of constant turbulence length scale L_T throughout the inlet section. The value of L_t was set equal to the pitch of the smoothing grid placed in the COULI apparatus upstream section (1.5 mm). Experimental measurements in section B-2 were used to assess the reliability of the above boundary conditions. Figure 4 shows the profiles of velocity and turbulence kinetic energy imposed in the inlet section and calculated in section B-2. Here, the agreement with experimental data is reasonably good, confirming the correctness of the assumption on L_t. Furthermore, residual errors related to the inlet conditions are smoothed down along pipe before the window region (which is about 10 diameters long).
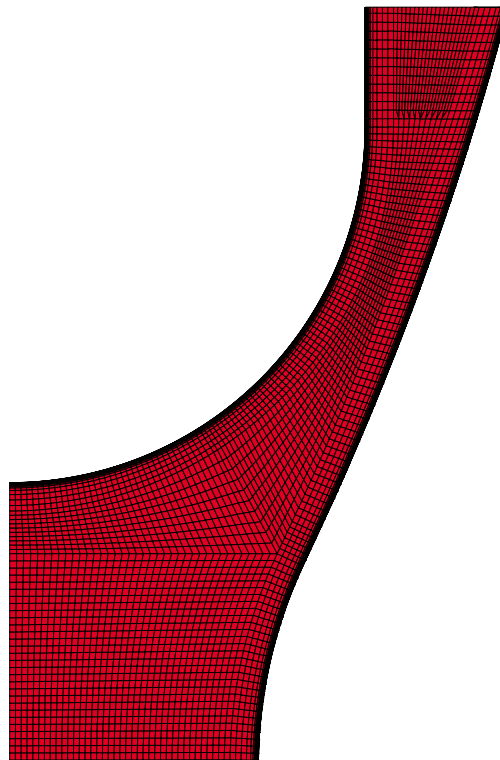

Figure 3 - Computational mesh in the window region for cases 1, 3 and 4.
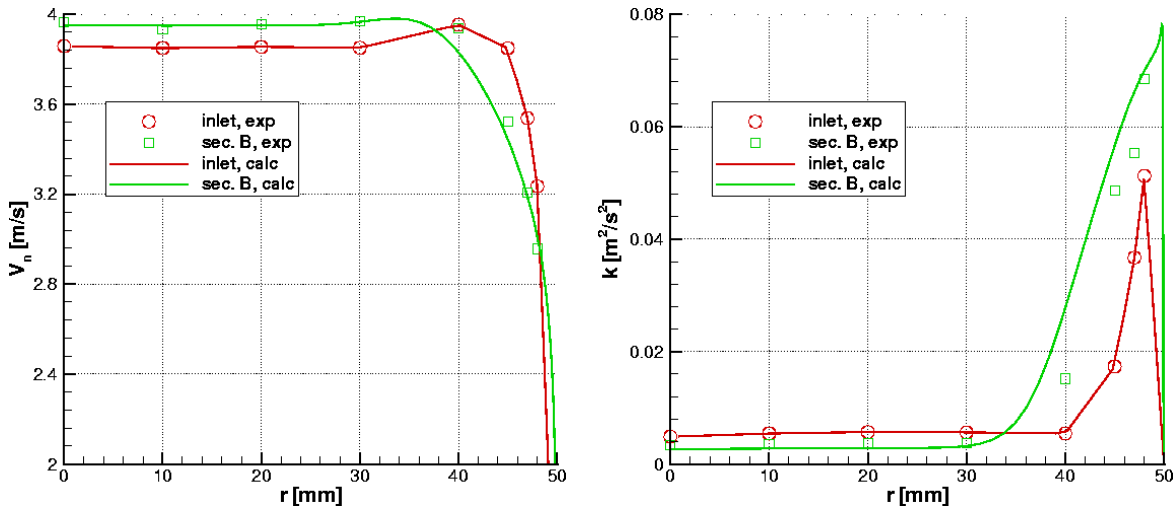
Figure 4 - Velocity (left) and turbulence kinetic energy (right) profiles in the inlet section (sec. A1, assigned from the experimental data, red lines) and in section B2 (green lines).

All simulations were run using the SIMPLE steady-state integration algorithm. Both the QUICK third-order and the MARS second-order scheme [6] were used, applied both to the momentum and to the turbulence equations (see also Sec. 3.4).

The Chen k-ε model [6] [7] was used for all the simulations, joined with a Norris & Reynolds two-layer one-equation model [6] for the near-wall turbulence. The grid requirements for a good performance of the latter are to have at least 15 cells in the layer resolved with the two-layer, with a maximum value of y^+ of about 3. The distribution of y^+ for case 1 is shown in Figure 5. The maximum value is 2.6 and can be found in the window wall were the maximum flow velocity is reached (see Sec. 3.3). Correspondingly, the minimum number of cells contained in the layer resolved by the two-layer is found to be 13. Higher values (up to 20) result elsewhere.
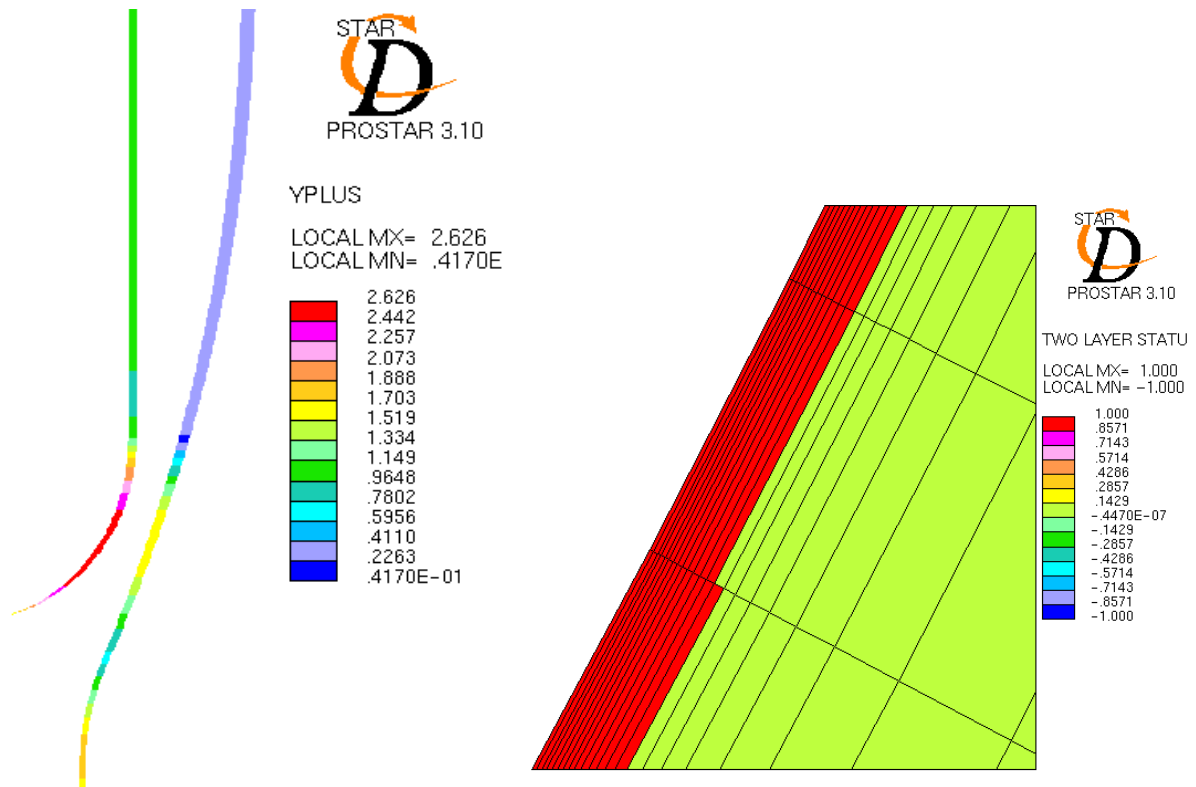
Figure 5 - Distribution of y^+ on the walls in the window region (left) and cell layer resolved with the two-layer model (in red) in the wall region at highest y^+ (right).

2.3 Calculation strategy

Four cases are presented in this report, as shown in Table 3. Case 1, run on a 2D geometry with the QUICK convective schemes, is the reference calculation. Case 2 was run with a doubled density mesh, in order to assess the grid independence of the results. Case 3 had the purpose of analysing the effect of using a different convective scheme (MARS). Case 4 was run with a full 3D model, obtained from the basic 2D model by circumferential extrusion of 72 1-cell-thick sectors of 5°. The purpose of this calculation was to check the possible arising of 3D flow instabilities in the diverging duct which could explain the strong lack of axis-symmetry of experimental results [8].

Table 3 - List of test cases.

	Topology	**Grid density**	**Convective schemes (momentum/k-ε)**
Case 1	2D	25,500	Quick/Quick
Case 2	2D	102,000	Quick/Quick
Case 3	2D	25,500	MARS/MARS
Case 4	3D	25,500 x 72 (1,836,000)	MARS/MARS

8

3 Results

3.1 Presentation of results

Results are presented both in form of field plots and in form of profiles of the flow variables in sections 3-9 (Figure 2). Flow-variables profiles are presented in non-dimensional form; the reference values used for the non-dimensionalisation are reported in Table 4. The abscissa along the various sections is also non-dimensional and is given by

$$x_{ad} = \frac{r - r_{min}}{r_{max} - r_{min}}$$

where r is measured in the cylindrical reference system coaxial with the test section for sections M,3 and from 6 to 9, and in spherical reference system of the window for sections 4 and 5.

Table 4 - Reference values for non-dimensionalisation; U is the inlet mean normal velocity (3.714) and D id the inlet diameter (=0.1 m).

Variable	Reference values
Velocity components	U
Turbulence kinetic energy and Reynolds stresses	$0.5\ U^2$
Turbulence dissipation	U^3 / D
Turublent cinematic viscosity	U D

Reynolds stresses are calculated according to the Boussinesq eddy-viscosity approximation for linear models [6], which for an incompressible axisymmetric flows yields [5]

$$\frac{\tau_{rr}}{\rho} = -\overline{v_r' v_r'} = 2\nu_t \frac{\partial v_r}{\partial r} - \frac{2}{3} k$$

$$\frac{\tau_{zz}}{\rho} = -\overline{v_z' v_z'} = 2\nu_t \frac{\partial v_z}{\partial z} - \frac{2}{3} k$$

$$\frac{\tau_{rz}}{\rho} = -\overline{v_r' v_z'} = \nu_t \left(\frac{\partial v_r}{\partial z} + \frac{\partial v_z}{\partial r} \right)$$

3.2 Convergence

The convergence histories for the considered cases are reported in Figure 6. The Star-CD default residuals normalisation is adopted, which uses as normalisation factors a representative flow rate of the considered variable in the domain [6]. For the continuity equation, the largest residual in the first ten iterations is adopted.

Only case 1 was run starting from scratch. Case 2 started from the solution of case 1 mapped on the fine mesh, case 3 restarted from case 1 and case 4 started from the solution of case 1 interpolated on the 3D domain. All the calculations have a satisfactory convergence level.
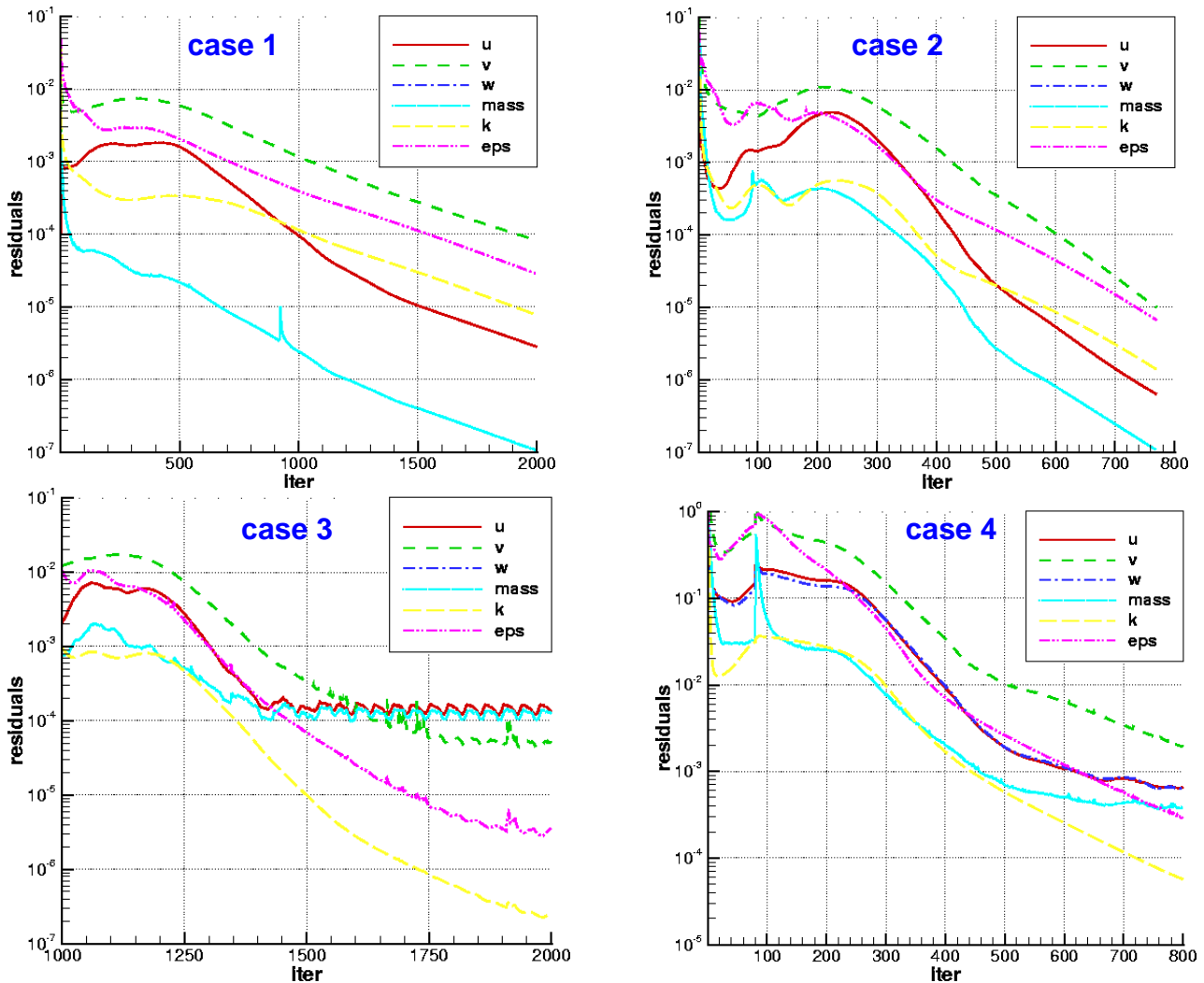
Figure 6 - Convergence history for cases (from top left) 1,2,3 and 4. Only in case 1 the calculation started from scratch, while all the other cases started using case 1 as initial field.

3.3   Flow field description (case 1)

The duct formed by the hemispherical window wall and by the external guide wall is a sort of 3D converging-diverging annular duct, where the combined effects of the different wall curvatures and of the diffusing effect of the radius increment result in a strongly non-uniform flow pattern.

The flow characteristics in the zone of interest are illustrated in Figure 7, where vector and contours plots of relevant quantities relative to case 1 are shown. For description purposes, the flow coming up from the inlet pipe can be divided into to halves: an internal stream (nearby the axis) and an external stream (nearby the guide wall). The internal stream is first slowed down, up the stagnation point on the window tip, with a consequent pressure increase, then it turns and accelerates along the window wall up to the maximum velocity (nozzle throttle) and slows down again in the diffusing riser. The external stream, containing the boundary layer formed along the inlet pipe, turns and slows down along the guide tube, until it detaches from the wall generating a recirculation region. The extension of the recirculating flow is visible in blue in the axial-component contour plot. These

10

two streams generate a shear layer with adverse pressure gradient in the first part of the riser, with intense turbulence generation and consequent decay, as it can be seen from the contour plots of k and ν_t in Figure 7.

The flow simulation is very challenging for turbulence models, due to presence of stagnation points, of boundary layers with adverse pressure gradient and strong shear components. In particular, a correct prediction of the turbulence generation in the stagnation region is crucial for a correct reproduction of the flow behaviour (detachment) in the diverging riser.

Profiles of velocity components, k, ε, ν_t and Reynolds stresses in the prescribed sections (also sketched in Figure 7) are reported in Figure 8, Figure 9 and Figure 10.
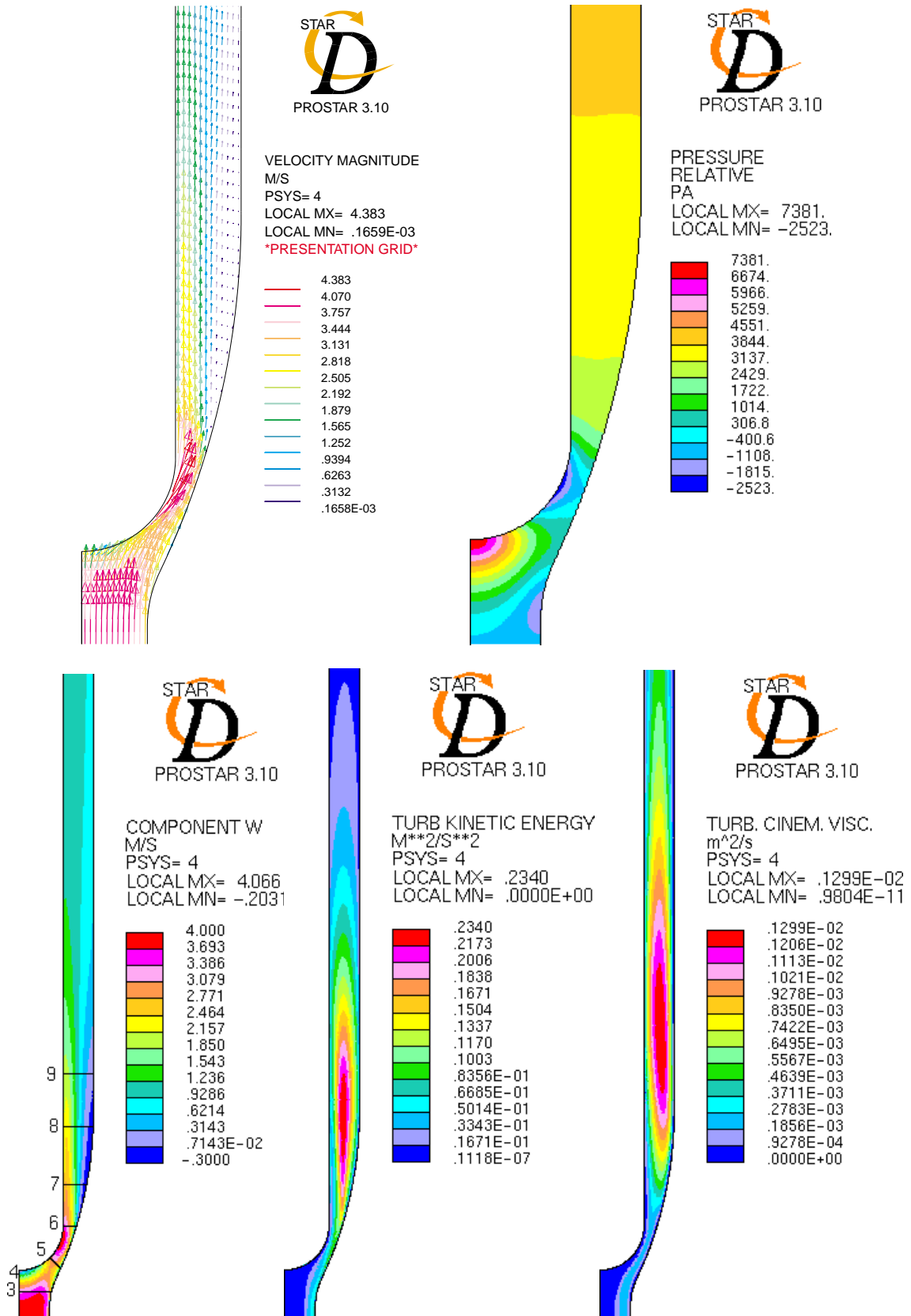
Figure 7 - Flow field description (from top-left): velocity vectors, pressure, axial velocity component (with the sketch of the probe sections), turbulence kinetic energy and turbulent cinematic viscosity fields.
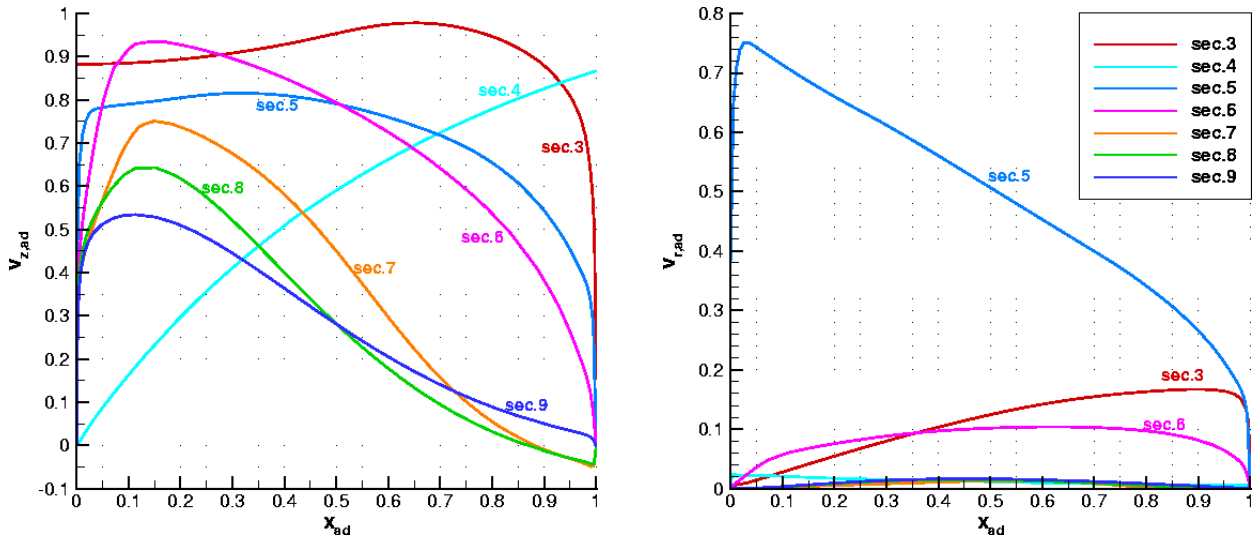
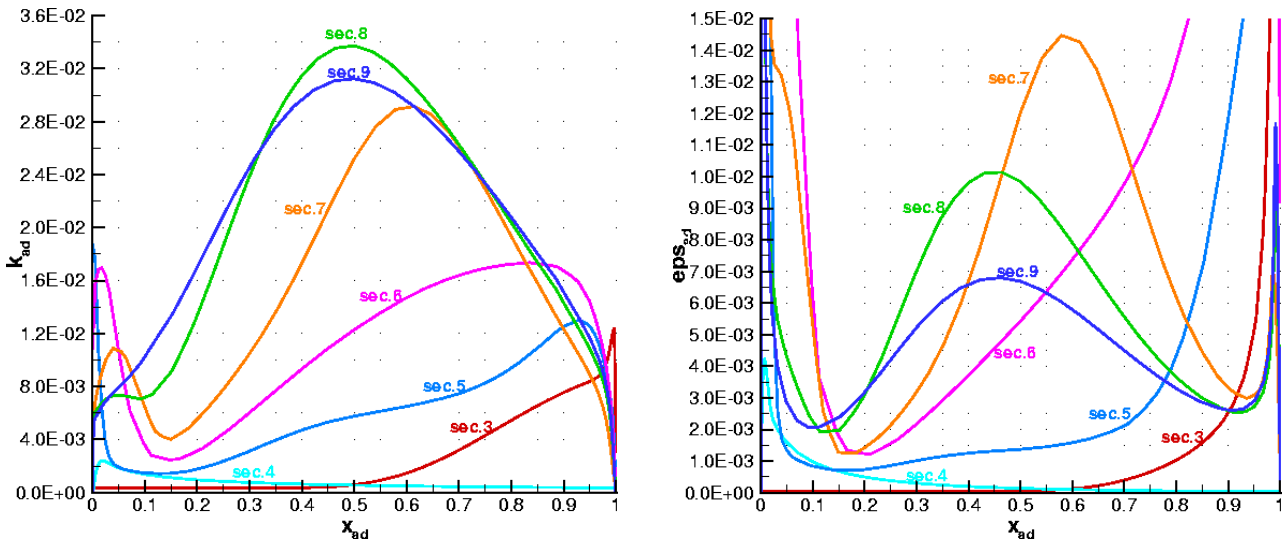Figure 8 - Axial (left) and radial (right) non-dimensional velocity profiles in sections 3-9.

Figure 9 - Non-dimensional turbulence kinetic energy (left) and dissipation (right) in sections 3-9.
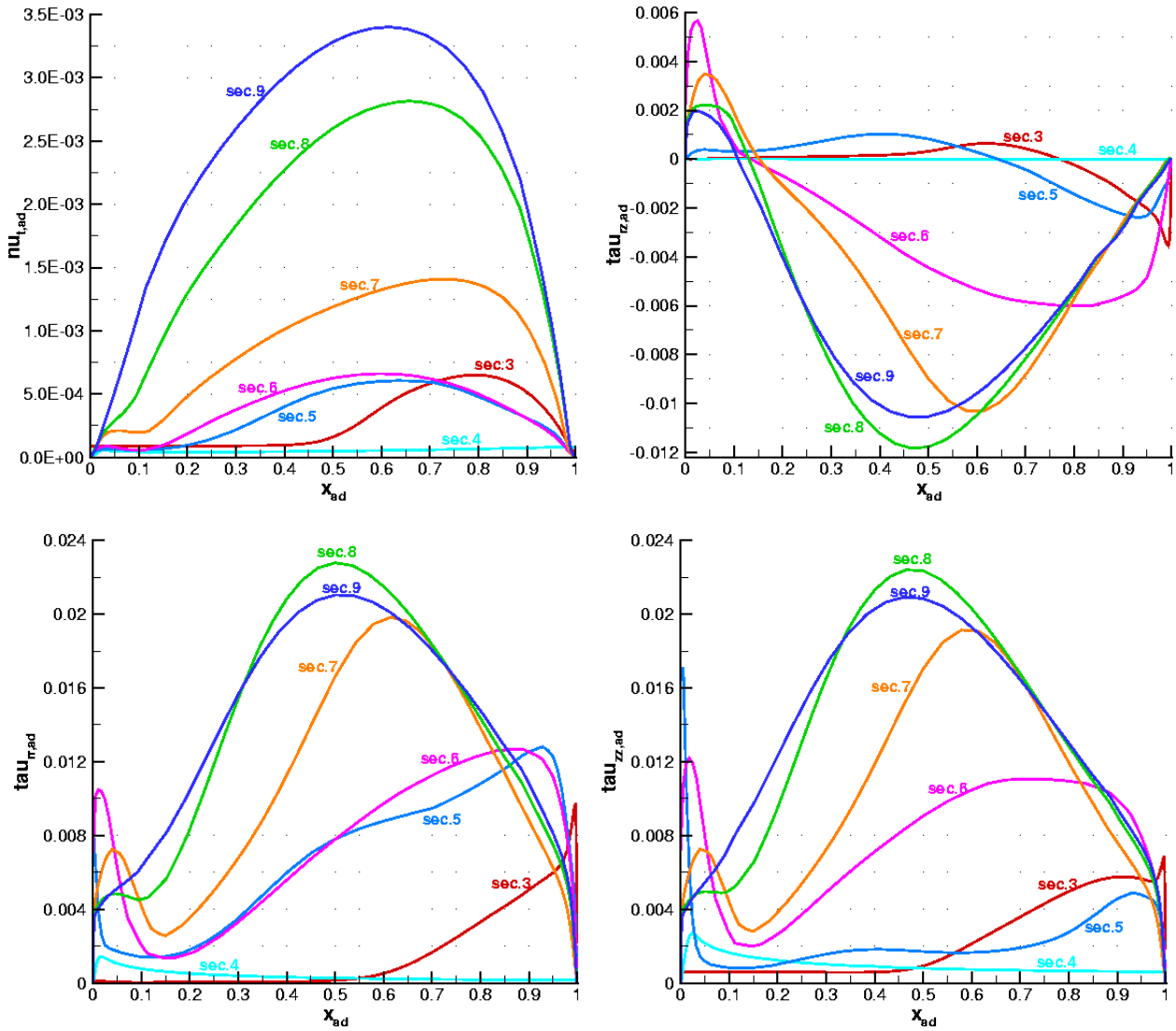
Figure 10 - From top-left: profiles of turbulent viscosity and of the three Reynolds stresses components (τ_{rz}, τ_{rr} and τ_{zz} respectively) in sections 1-9.

3.4 Grid and scheme independence (Cases 1-2, 1-3)

The solution obtained in case 1 is compared with case 2, run with a double mesh density, in Figure 11 (left), where the profiles of axial velocity and turbulence kinetic energy are compared in section 8. The agreement is quite satisfactory; just a little difference can be observed in the velocity profile, with a maximum error of about 0.1 %.

The graph on the right of Figure 11 shows the effect of using a different convection scheme for both the momentum and the turbulence equations. Results are practically identical.
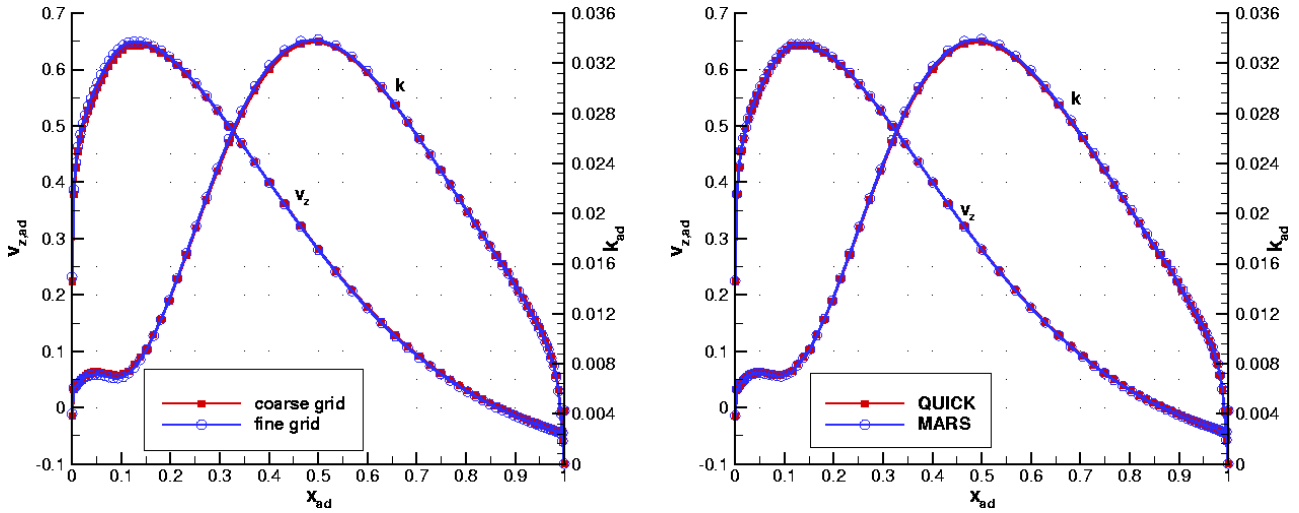
Figure 11 - Profiles of axial velocity component and turbulence kinetic energy in section 8: comparison between cases 1 - 2 (left, grid-independence) and 1 - 3 (right, scheme independence).

3.5   3D effects

Case 4 was run to check possible three-dimensional instabilities intrinsic in the flow morphology. It was not possible to run this case with the QUICK scheme, which gave rise to numerical instabilities. No problems were encountered with the MARS scheme.

The fact that it was possible to obtain a converged steady solution already demonstrated that no oscillatory phenomena were reproduced by the numerical simulation. The axial symmetry of the solution is confirmed by Figure 12, which shows contours plots of the three velocity components and of the turbulence kinetic energy in section 8.

Figure 13 shows the comparison with the 2D case run with the MARS scheme (case 3). No appreciable differences can be observed.
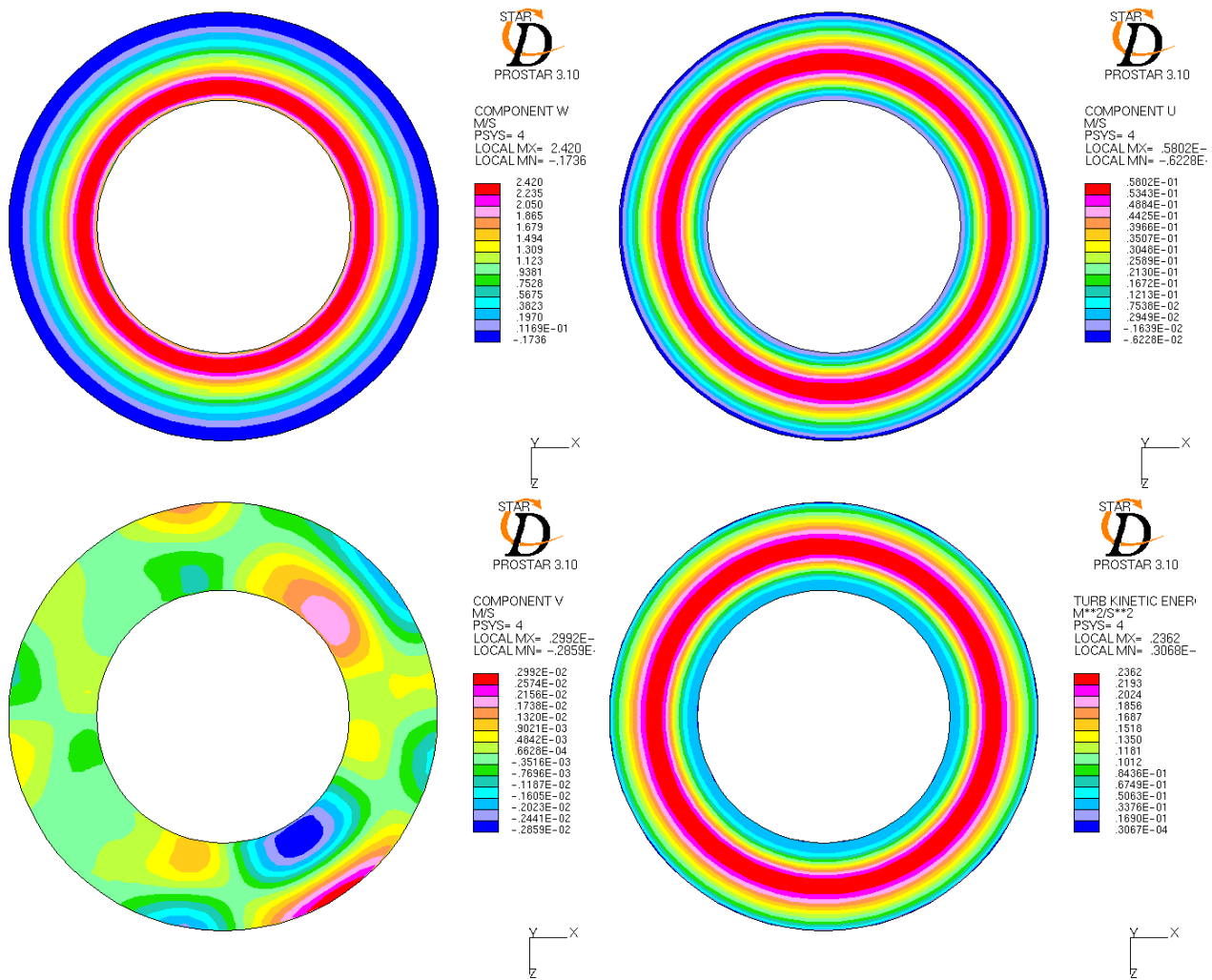
Figure 12 - Case 4: distribution of (from top-left) axial, radial and tangential velocity components and of turbulence kinetic energy in section 8.
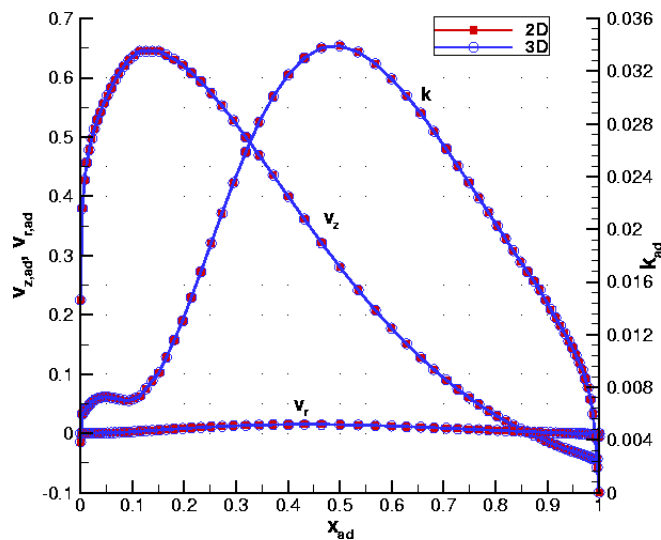

Figure 13 - Profiles of axial and radial velocity component and turbulence kinetic energy in section 8: comparison between cases 3 and 4.

3.6 Comparison with experimental results

Although measurements of both mean and fluctuating velocity components were performed, only axial velocity measurements in sections M, 8 and 9 were available at the time this report was written.

Experimental measurements were performed at different azimuthal positions. Results showed a strong lack of axial-symmetry, as shown in Figure 14, where the axial velocity field on section 8 is plotted as a function of the radius and of the azimuthal angle. For example, at a constant radius of 94 mm, a variation from 0.6 to1.8 m/s can be observed along an arc of 180°, which corresponds to a deviation of 120 % from the mean value (about 1 m/s). A much lower effect was observed in section M upstream the window, where the deviation was about 10 %. Considering that a stationary flow was observed [8], the cause of this variation is probably a lack of symmetry in the apparatus.

For benchmarking purposes, azimuth-averaged values, scaled with the volume flow rate, were supplied by CEA. However, this problem should be taken into account when evaluating computational results.
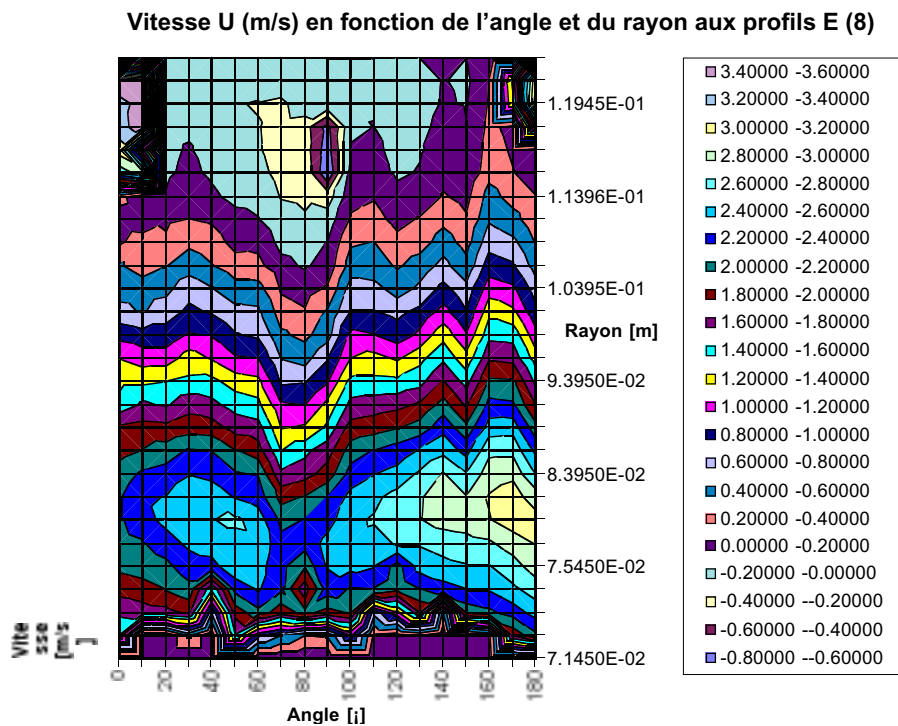

Figure 14 - Experimental measurements of the axial velocity component (values are in m/s) in section 8 as a function of the azimuth and of the radius.

Figure 15 shows the comparison between experimental and computed axial velocity profiles in sections M, 8 and 9. In spite of the above-mentioned problem, results are in reasonable agreement. The following things can be observed:

- experiments show an upstream effect of the window already in section M, where a slightly deformed velocity profile can be observed, while the numerical profile is still unperturbed. A

profile with similar shape can be found in a section downstream at z=-65 mm from the window tip. However, even in this section the experimental profile is slightly higher with respect to the numerical one, which could imply some problem with the flow rate conservation, having considered that lateral walls are still straight at this level.

-   Profiles in section 8 are in very good agreement, demonstrating the capability of the turbulence model to predict correctly the flow detachment along the diverging duct.

-   The turbulence decay along the riser seems to be overestimated by the code, as revealed by profiles in section 9, where a flatter experimental profile can be observed.

In general, results confirmed the capability of the code to reproduce the main flow characteristics.
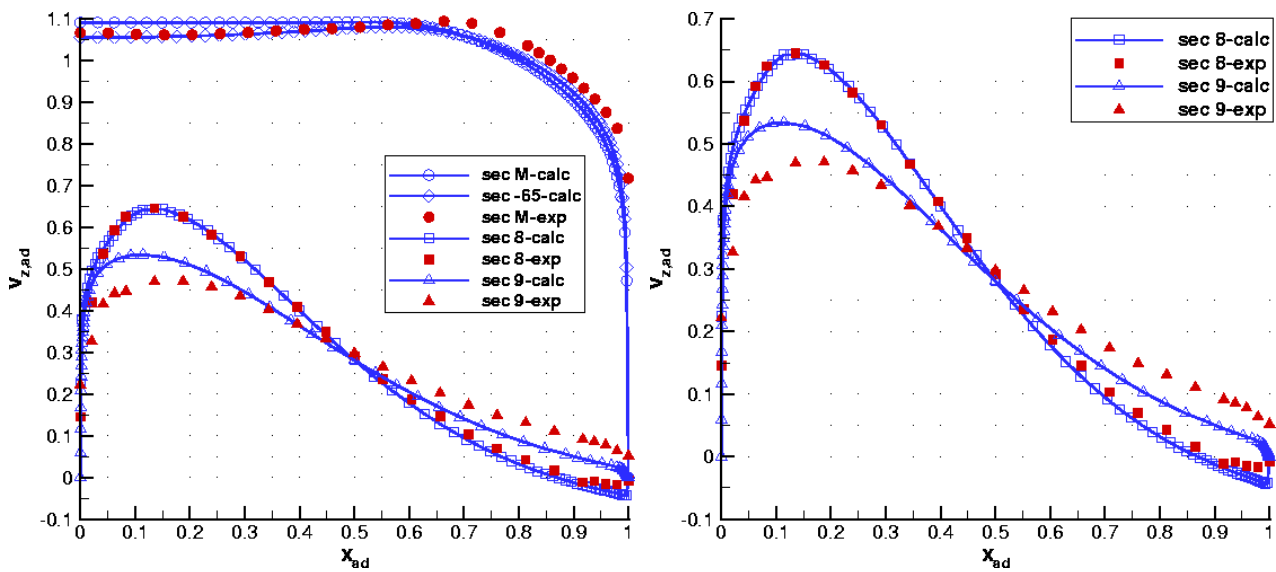

Figure 15 - Case 1: comparison between experimental and calculated axial velocity profiles in sections M, 8 and 9 (left) and in sections 8 and 9 only with different scale (right). The computed profile in a section at z= -65 mm are also reported.

4 Conclusions

The COULI experiment, consisting of an isothermal water-flow in a geometry typical of the spallation target of the Italian ADS target, was simulated using the Star-CD commercial code, with a Chen k-ε high-Reynolds model joined with a Norris & Reynolds Two-Layer model.

The grid-independence of the solution has been verified, and the results obtained with two different convection schemes (QUICK and MARS) has been compared, in order to minimise numerical uncertainties. No appreciable differences were found in the results.

A full 3D calculation did not revealed any 3D instability intrinsic in the flow morphology.

Some problems were encountered in the experimental measurements due to the lack of axial symmetry of the experimental set-up. In spite of this, the comparison with computational results showed the capability of Star-CD, using the Chen k-ε model, to correctly simulate the main flow characteristics.

5 References

[1] C. Aragonese, S. Buono, L. Maciocco, V. Moreau, L. Sorrentino, "*A Beam Window Target Design with Independent Cooling for the EADF*", CRS4 Technical Report 00/85

[2] V. Bellucci, S. Buono, L. Maciocco, V. Moreau, L. Sorrentino*, "Proposal for the fluid-dynamic simulation of the target geometry for the COULI experimen"t*, CRS4 Internal note, November 1999.

[3] L. Carteciano, X. Chen, B. Dorr, G. Grötzbach, L. Maciocco, "*Report of the preliminary calculations of the COULI benchmark*", January 2000.

[4] Y. Dolias, L. Maciocco, P. Roubin*, "Proposal for the CFD benchmarking activity on the COULI experiment*", June 2002

[5] E. B. Bird, W. B. Stewart, E. N. Lightfoot, "*Transport Phenomena*", Wiley & sons, 1976

[6] Star-CD v3.05 User Manual (Methodology volume), Computational Dynamics Limited, 1998.

[7] Y.S. Chen, S.W. Kim, "Computation of turbulent flows using an extended k-ε turbulence closure model", NASA CR-179204, 1996

[8] CEA information

[9] L. Maciocco, M. Mulas, "Analysis of Star-CD Numerical Performances", CRS4 Internal Note 5-97, 1997.